

Landmine detection with an imaging 94 GHz radiometer

Jos Groot, Rob Dekker, Lucas van Ewijk

TNO Physics and Electronics Laboratory, P.O. Box 96864, 2509 JG The Hague, The Netherlands

ABSTRACT

We analysed a time series of 94 GHz radiometer images of a sandbox with buried and unburied, metal and plastic AP and AT dummy mines. The images covered almost a complete 24 hour cycle, with both clear sky and rain conditions occurring. The AP nor the buried mines were visible at any time. The contrast of the visible mines depended mostly on the sky conditions. The plastic mines were (almost) always brighter than the background, the metal mines darker.

Keywords: landmine, detection, microwave, radiometer

1. Introduction

Mine detection can be done with imaging sensors operating at different wavelengths. Short wavelength sensors, like infrared cameras, are generally capable of detecting unburied mines only. Only through indirect effects these sensors are able to detect buried mines at certain times of the day. For time independent buried mine detection one needs longer wavelengths, in the mm-dm range (mm/microwave sensors). Candidate mm/microwave sensors for landmine detection are radars and radiometers. Most of the research to date focuses on (ground penetrating) radar. However, a radiometer has some advantages when compared to radar. One of those is that it is less sensitive to the mine orientation than radar. A radiometer's drawback is its relatively low spatial resolution. By using a sufficiently high frequency and a large antenna this is no problem at short ranges.

Recent studies demonstrated the possibility of detecting both buried metal (at 44 GHz)¹ and unburied metal/plastic (at both 35 and 90 GHz)² mines with mm-wave radiometers, at short distances. These studies were done with non-imaging radiometers during daytime. The main goal of the present study was to assess the performance of an imaging radiometer, compared to visual and IR sensors. To meet this objective, images of a simulated minefield obtained during a complete 24 hour cycle were analysed with respect to the mine-background contrast. This paper presents the mm-wave image analyses, the visual/IR data analyses are given in³.

2. Microwave radiometry

2.1. Radiometer

A microwave radiometer measures the total power entering it from the direction its antenna is pointing to⁴. Assume that a radiometer is looking downward at terrain. The received power consists of three contributions:

1. power emitted by the terrain
2. power emitted by the atmosphere and then reflected by the terrain
3. power emitted by the atmosphere between the radiometer and the terrain

In the remainder of this paper we will neglect the third contribution, because in our case the radiometer-terrain distance was small (≈ 20 m). If the radiometer is properly calibrated, the received power can be converted to an apparent temperature. The apparent temperature corresponding to the sum of the first and second contribution is

$$T_a = eT + (1 - e)T_{sky}, \quad (1)$$

in which T_{sky} denotes the apparent temperature of the sky (sky temperature) and T the physical (thermodynamic) terrain temperature. We used the fact that the reflection coefficient equals 1 minus the emissivity e .

2.2. Sky apparent temperature

The main components of sky emission are due to emission by water vapour and molecular oxygen. The sky temperature increases with increasing zenith angle, due to the longer path length. It also increases with increasing cloud cover.

The effective sky temperature reflected by an object depends on the surface roughness. For a perfectly smooth object this is the specular sky temperature. For a perfectly rough (Lambertian) surface it is the sky temperature averaged over all directions. The effective sky temperature is then approximately $T_{skyd} \equiv T_{sky}(\theta=55^\circ)$ ⁵.

Table 1 shows calculated sky temperatures for various weather conditions. $\theta \approx 68^\circ$ is the average incidence angle at the mines during our experiment. The values agree reasonably well with the measurements reported elsewhere⁶.

<i>weather condition</i>	T_{skyd} [K]	$T_{sky}(\theta \approx 68^\circ)$ [K]
clear sky	67	95
moderate cloud cover	150	200
moderate rain	270	225

Table 1: Sky apparent temperatures⁵.

2.3. Apparent temperature contrast

Assume that a mine with emissivity e_m and temperature T_m lays on a sand background with emissivity e_s and temperature T_s . A radiometer measures the apparent temperature T_a of the mine. Generally, the mine will not completely fill the antenna beam. The measured apparent temperature therefore incorporates a contribution from both the mine and the background. The beamfill factor b accounts for this effect. Furthermore, the reflection from the sky (apparent temperature T_{sky}) by both the mine and background will contribute, too. The measured apparent temperature is

$$T_a = be_m T_m + b(1 - e_m)T_{sky} + (1 - b)e_s T_s + (1 - b)(1 - e_s)T_{sky}. \quad (2)$$

The terms from left to right are due to mine emission, mine reflection, background emission and background reflection, respectively. The apparent contrast temperature between the mine and the background is

$$T_c = T_a(b) - T_a(b=0) = b(e_m T_m - e_s T_s + (e_s - e_m)T_{sky}). \quad (3)$$

The contrast decreases with decreasing beamfill factor. Assumptions made in the derivation are:

1. the temperature of the mine and background are constants (in space). This is only approximately true. For example, shadowed parts of the mine will be relatively cold.
2. the mine and background emissivities are constants (in space).
3. the sky apparent temperature reflected by the mine and the background is the same. This is only approximately true, because this depends on the roughness of the mine and the background.

The effect of these approximations is that one has to use average, effective (apparent) temperatures and emissivities in the previous equations.

3. Mine detection experiment

3.1. Hardware

The hardware used consisted of a

- 94 GHz radiometer
- pedestal, movable in elevation and azimuth
- HP 9000 computer
- HP 6942A multiprogrammer, incorporating 2 DA (digital to analog) and 3 AD (analog to digital) converters, and a card with 4 digitally controllable relays.

The radiometer is mounted on the pedestal. The pedestal movement is controlled by the HP 9000 computer in conjunction with the 2 DA converters and 4 relays. The pedestal position is read out through 2 AD converters, which read potentiometers connected to the elevation and azimuth axes of the pedestal. Finally, an AD converter is used to digitise the radiometer signal, which is linearly proportional to the apparent temperature of the scene imaged. Radiometer characteristics are given in Table 2.

antenna	parabolic (radius 205 mm)
3 dB beamwidth	0.55°
type	Dicke switched radiometer
polarisation	horizontal
centre frequency	94 GHz
bandwidth	1.5 GHz
low pass filter frequency	10 Hz

Table 2: Radiometer characteristics.

Radiometer calibration with a temperature controlled matched load provided the linear relation (slope 20.88 mV/K) between voltage and apparent temperature.

3.2. Software

A HP9000 BASIC program used the following steps to measure an image:

1. ask the operator to point the radiometer to the upper left corner of the scene to be imaged.
2. scan line 1 from left to right (looking at the back of the radiometer) with an azimuthal angular speed of 2.75°/sec..
3. move 0.5° down.
4. scan line 2 from right to left.
5. repeat step 3.
6. repeat the above steps 2-5 until 100 lines are measured (each line contains about 270 pixels).

The radiometer output is sampled at the highest possible speed when scanning a line. The samples obtained during a sample time interval $\Delta t=0.0667$ sec. (corresponding to $0.18^\circ = 1/3$ resolution cell width ($=0.55^\circ$)) are averaged and stored in RAM. This additional averaging is done to reduce any radiometer and AD quantisation noise. About 6 samples were averaged for each 0.0667 sec. interval. The azimuth and elevation position samples are stored in RAM together with each radiometer sample. After a measurement all these data were saved in a file. The measurement of a single image took about 50 minutes.

3.3. Experimental setup

The test area was located in the dunes near TNO-FEL, the Hague, The Netherlands. The radiometer was put on a platform, with the radiometer antenna at a height of 7.6 m above the ground. The horizontal distance between the radiometer and the simulated minefield was about 19 m. The incidence angle at the mines ranged from 66-70°. Figure 1 shows the setup, looking at the back of the radiometer.

The minefield sandbox is visible in the lower part of the picture, below the radiometer. The bright metal strip at the left was lined up with the radiometer line-of-sight. It served as a reference for data pre-processing. Other reference targets were three square metal plates with 10, 30 and 50 cm side lengths put at the far end of the minefield.

The minefield contained metal and plastic anti-personnel (AP; size 5-10 cm) and anti-tank (AT; size about 25 cm) mines as well as some potential false alarm targets (a rock, a tile, a metal can, a hole and some glass). The unburied configuration at the left was repeated in the right half of the minefield, covered by a 3-4 cm thick sand layer (not visible in Figure 1).

3.4. Data acquired

3.4.1. Radiometer data

Table 3 shows some characteristics of the images measured with the radiometer.

The filename consists of the measurement date and the image sequence number. For example, data23_4 was the fourth image measured on August 23 1995. Some images are missing (e.g., data23_3), due to malfunctioning of the pedestal.

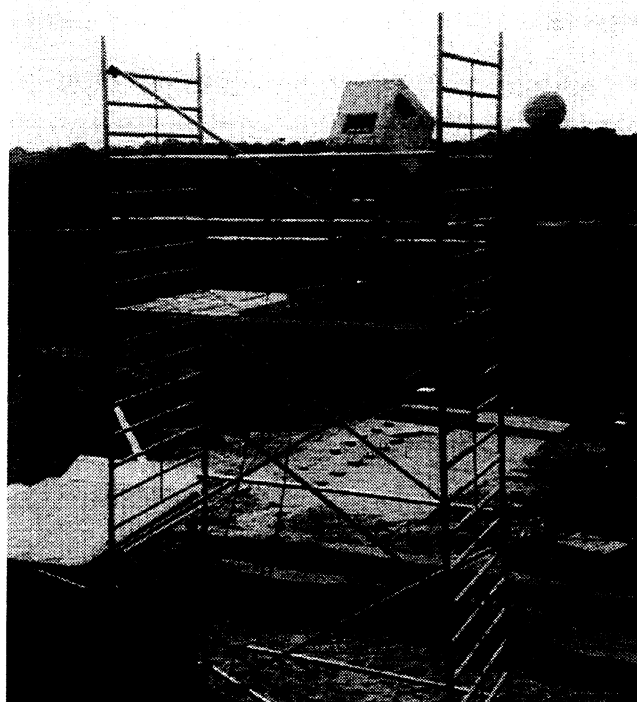


Figure 1: Experimental setup.

<i>filename</i>	<i>start time [hh:mm]</i>	<i>end time [hh:mm]</i>	<i>remark</i>
data23_2	14:36	15:26	-
data23_4	18:05	18:55	-
data23_5	20:03	20:54	-
data23_6	21:02	21:52	-
data23_7	22:00	22:54	-
data23_8	23:07	00:01	23:45-24:00 h: heavy shower
data24_1	01:08	02:02	-
data24_2	02:17	03:11	-
data24_3	03:22	04:16	-
data24_4	04:30	05:24	-
data24_5	05:36	06:30	-
data24_7	08:33	09:27	-
data24_8	09:38	10:32	-
data24_9	11:42	12:35	sand removed from buried mines

Table 3: Radiometer image data characteristics.

3.4.2. Weather data

A weather station measured the local air temperature, wind direction and speed, relative humidity, sun energy flux, atmospheric pressure and rain rate (unfortunately, the rain sensor turned out to be defect). Because the sky temperature depends heavily on

the amount of cloud cover, this is an important parameter. Between sunset and sunrise the cloud cover can evidently not be retrieved from the sun flux data. We therefore asked a meteorological station at 9 km distance from the test site for a cloud cover estimate (Figure 2).

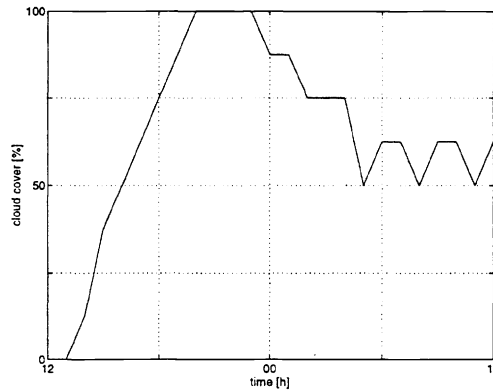


Figure 2: Cloud cover data.

The cloud cover is a percentage between 0 and 100 (steps of 12.5 %), denoting the percentage of the sky blocked by clouds. Because it is an average of 3 similar figures for cloud cover at three different heights, it is also related to the thickness of the cover.

3.4.3. Thermocouple data

The temperatures of the targets and the sand background were measured with thermocouples. The apparent temperature contrast between a mine and the background depends on, among other factors, the temperature difference between the mine and the background. The mine temperatures minus the sand surface temperature are shown in Figure 3.

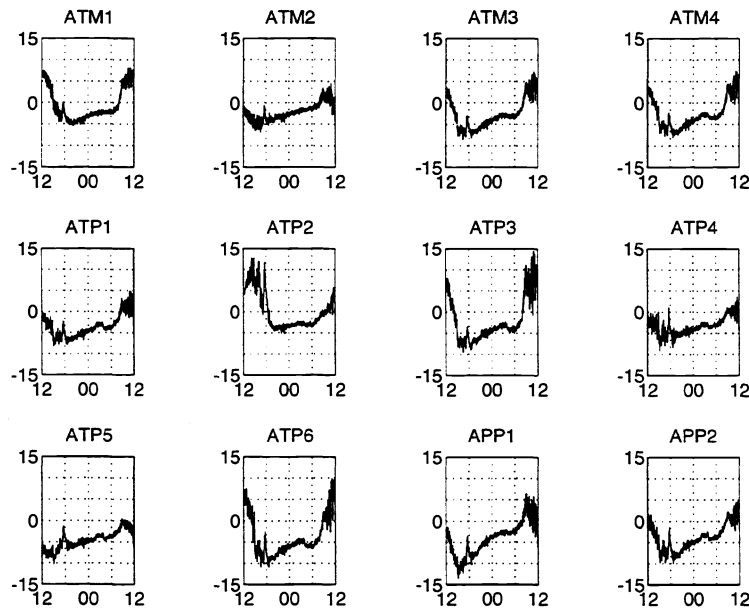


Figure 3: Thermocouple temperature contrasts. Time period: Aug. 23 12:00 h to Aug. 24 12:00 h. ATM= AT metal casing; ATP= AT plastic casing; APP= AP plastic casing.

The time axis as used in these plots covers the time interval of August 23 12:00 h to August 24 12:00 h. For reasons of compactness we omitted the x - and y -axis labels. This format also occurs in some subsequent plots. The average trend is a contrast decrease between 12:00 h and 18:00 h, then a gentle increase from 18:00 (August 23) to 6:00 h (August 24), and finally a faster increase from 6:00 to 12:00 h. During this last period the differences varies considerably due to clouds. The mines can be divided in two classes, depending on the average variation in the difference data. ATM2, ATP4, ATP5 and, to a lesser extent, ATP1 exhibit a relatively small variation. The casing and filler of ATM2 (aluminum) and ATP1 (plastic) are both identical, while ATP4 and ATP5 consist of cast explosives. This suggests that "homogeneous" mines adapt themselves faster to the temperature of the surroundings than non-homogeneous mines.

4. Data analysis

4.1 Data preprocessing

The raw radiometer and azimuth/elevation sample data were converted to rectified apparent temperature images by the following steps:

1. reverse the left-right ordering of lines 1, 3, 5, ..., 99. This compensates for the alternating left-right/right-left scanning order.
2. resample (nearest neighbour method) the radiometer samples of all lines by a polynomial (8th degree) fitted through the azimuth position samples. This compensates for scan speed variations, and assures that the distance between samples in a line is a constant.
3. shift the radiometer lines by an offset obtained from the correlation of the response of the metal strip with a Gaussian pulse. After this, the pedestal overshoot is compensated, and the metal strip appears straight in the image.
4. convert the voltage image to an apparent temperature image with the calibration data.

The images now have the same scales, spatially as well as radiometrically, and can be compared. Due to the 0.55° antenna beamwidth the horizontal (cross-range) and vertical (slant range) resolution at the mines are about 20 and 50 cm, respectively. To ease location of the mines, the images were stretched radiometrically. The applied stretching algorithm divides an image in a low-frequency and a high-frequency image, stretches the histograms of these two images separately, and combines them again⁷. Figure 4 shows a contrast stretched image. The metal strip is clearly visible as a vertical dark line at the left. The 50 cm reference target is at the top image. Some of the unburied mines are hot (bright) compared to the background, other mines cold (dark). The AP mines and buried mines are invisible.

4.2. Temperature resolution

An estimate of the temperature resolution of the data was made by computing the standard deviation of the pixel values over 5 visually homogeneous areas in data23_4. The average was 0.69 ± 0.08 K. This agrees well with the 0.79 K predicted using system parameters and the 0.70 K measured in the past⁸.

4.3. Apparent temperatures - qualitative analysis

Figure 5 shows the complete time series of 14 images. Careful inspection revealed that the AP and the buried mines were invisible at any time. The contrasts of the visible (unburied AT) mines and the potential false alarms were estimated by subtracting the time dependent apparent temperature of a homogeneous patch of sand from the respective temperatures. The result is provided by Figure 6.

The contrasts of the mines are between -17 and +12 K. The mines and potential false alarms can be divided in 3 classes:

- | | |
|---------------------------------------|---|
| 1. contrast always positive: | all plastic mines and the rock, tile and hole potential false alarms. |
| 2. contrast (almost) always negative: | all metal mines (except ATM1) and the glass. |
| 3. contrast negative or positive: | a metal mine with a rubber bumper (ATM1) and the metal can. |

The potential false alarms cannot be discerned from the mines.

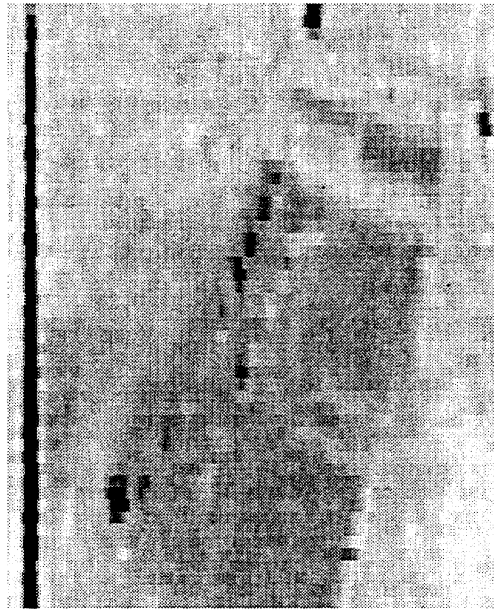


Figure 4: Contrast stretched data23_2 image.

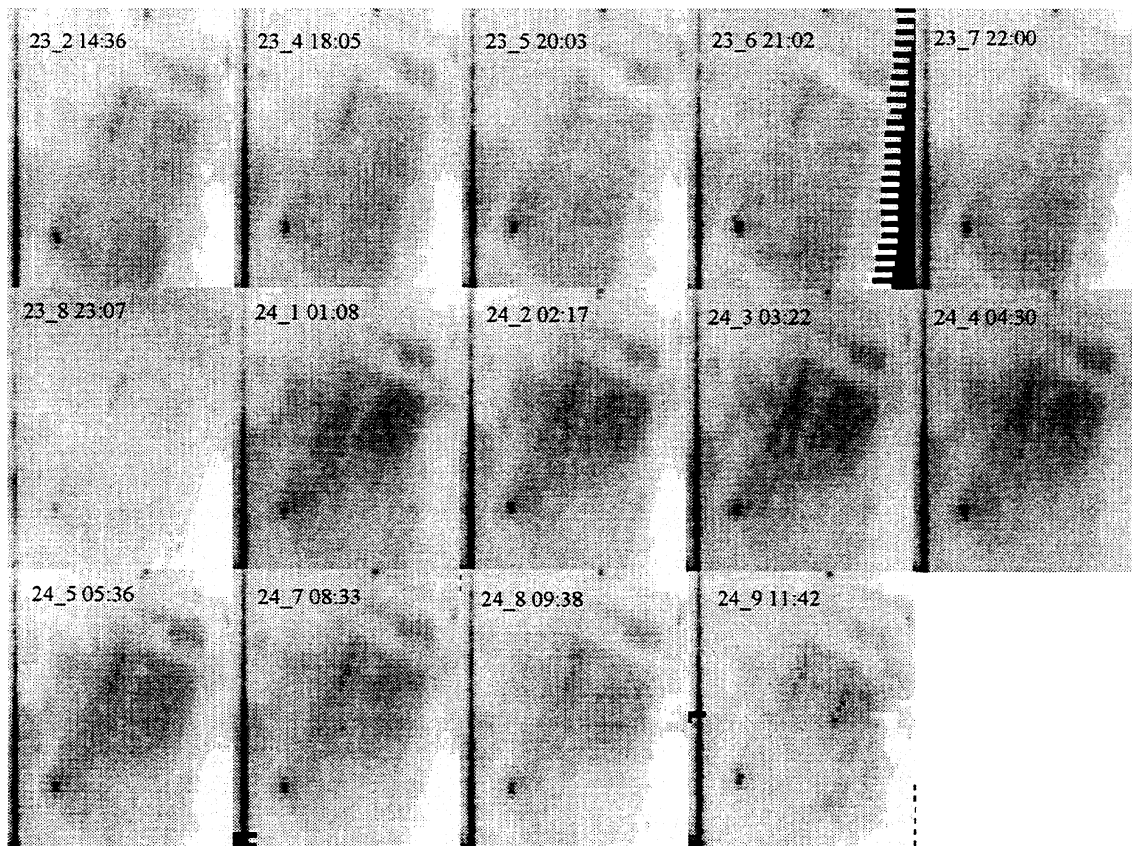


Figure 5: Time series of 14 images.

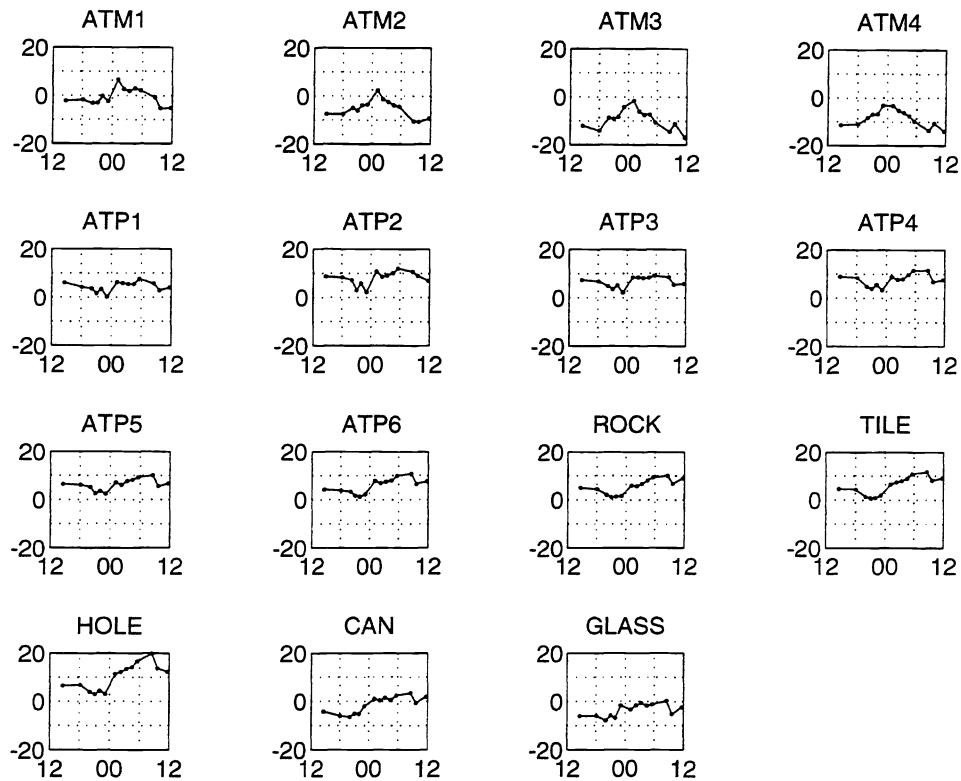


Figure 6: Apparent contrast temperatures of unburied mines and potential false alarms.

4.4. Apparent temperatures - quantitative analysis

Eq.(3), the theoretical mine-sand background apparent contrast, can be rewritten as

$$T_c = b(e_s(T_m - T_s) + (e_m - e_s)(T_m - T_{sky})). \quad (4)$$

Because the mine-sand temperature contrast ($T_m - T_s$) is relatively small (Figure 3), this is approximated by

$$T_c \approx b(e_m - e_s)(T_m - T_{sky}). \quad (5)$$

The validity of this approximation is supported by these observations:

- the mine-sand temperature difference has a minor influence on the apparent contrast: there are no clear correlations between Figure 3 and 6.
- the sign of the apparent contrast depends on the sign of $(e_m - e_s)$, since the mine temperature always exceeds the sky temperature: this is confirmed by the contrast classification of Section 4.3: the apparent temperature of the metal mines is lower than that of sand at all times, that of the plastic mines is always higher.
- the apparent contrast gets worse (smaller) with increasing sky temperature: this is true for all mines (Figure 6), especially during the shower around midnight. The contrast reduction is larger for metal than plastic mines, probably due to the larger difference between e_m and e_s for the metal mines.

We tried to explain the observed apparent contrasts by substituting reasonable values for the sky temperatures (Table 1; assuming specular reflection) in Eq.(4). The mine and sand temperatures used are from our own thermocouple measurements, while

the beamfill factor is on average 0.65 (computed from the theoretical antenna pattern). The sand emissivities are taken from⁹. The result is provided in Table 4. The contrasts between (...) were computed with the approximate Eq.(5).

<i>mine</i>	<i>weather</i>	e_m	e_s	$T_{sky} [K]$	$T_m [K]$	$T_s [K]$	$T_c [K]$
plastic	moderate rain	0.95	0.90	225	292	310	-8.4 (2.2)
plastic	clear sky	0.95	0.90	95	315	318	5.4 (7.2)
metal	moderate rain	0.0	0.90	225	292	310	-50 (-39)
metal	clear sky	0.0	0.90	95	315	318	-130 (-129)

Table 4: Computed (estimated) apparent contrasts.

The order of magnitude (but not the sign for moderate rain) of the computed contrasts agrees with the measured contrasts for the plastic mines. The measured (absolute) metal mine apparent contrast is much lower than the predictions. This is possibly due to the emissivity of the mines being larger than 0.0. All metal mines had a paint layer with a thickness of 0.05 mm, which leads to a layer of $0.05/\cos(70^\circ) \approx 0.15$ mm as observed by the radiometer.¹⁰ gives measured emissivities (at 94 GHz and normal incidence) of 0.040 and 0.098 for bare and painted metal, respectively. This painted metal value is still too small to explain our measurement. An emissivity $e_m=0.81$ is needed to get $T_c=-15$ K during clear sky conditions.

4.5. Sky temperature estimation

According to Eq.(1) the apparent temperature due to emission and sky reflection is

$$T_a(x, y) = e(x, y)T(x, y) + (1 - e(x, y))T_{sky}(x, y), \quad (6)$$

where we made the dependence on the position (x, y) in the scene explicit. The variation of $T_a(x, y)$ over the scene, ΔT_a , is given by the total differential of $T_a(x, y)$,

$$\Delta T_a = (T - T_{sky})\Delta e + e(\Delta T - \Delta T_{sky}), \quad (7)$$

in which Δe , ΔT and ΔT_{sky} represent the in-scene variation of the emissivity, the temperature and the sky temperature, respectively. We estimate the quantities at the right side of this equation as follows:

- $T \approx 280-330$ K
- $T_{sky} \approx 80$ (clear sky)-250 (rain) K (Table 1)
- $e \approx 0.8-1.0$
- $\Delta T \approx 15$ K
- $\Delta T_{sky} \approx 25$
- $\Delta e \approx 0.2$. The small emission coefficient of the metal mines and strips is unimportant, because these cover only a small fraction of the scene.

It follows that under most weather conditions Eq.(7) can be approximated by

$$\Delta T_a = (T - T_{sky})\Delta e. \quad (8)$$

This implies that the scene contrast as caused by emissivity variations across the scene decreases with increasing sky temperature.

It is possible to estimate the sky temperature for the 14 images with Eq.(8). Assume that the sky temperature was 80 K (clear sky) during measurement 1. Together with the measured apparent temperature variation ΔT_a and thermocouple temperature T of the sand surface it is possible to compute Δe for this image. If we assume this to be a constant for all images (which is valid if rain decreases the emission coefficient of all materials with approximately the same amount), this gives an estimate of T_{sky} for the 13 remaining images:

$$T_{sky} = T - \frac{\Delta T_a}{\Delta e}. \quad (9)$$

The result is provided in Figure 6. The solid curve results from estimating ΔT_a by the average of the absolute differences between the apparent temperatures (of all pixels) and the average apparent temperature of an image (which is 2.1 to 7.6 K). Estimation by the maximum minus the minimum apparent temperature (right figure of Figure 6) leads to the dotted curve.

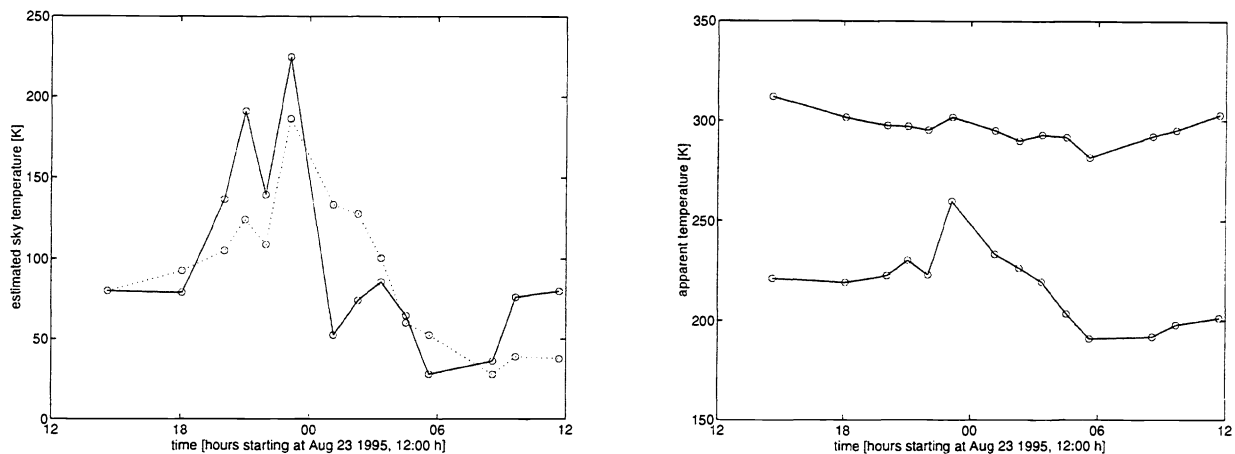


Figure 6: Estimated sky temperatures (left plot). Maximum (top) and minimum (bottom) apparent temperatures (right plot).

The estimations agree reasonably well with the cloud cover data of Figure 2, and correlate well with the apparent contrasts of Figure 6. The probable underestimation of the sky temperature after midnight is probably due to underestimation of Δe : the sand minefield is generally darker than the surrounding grass/moss. This difference increases after the shower shortly before midnight, indicating a change in Δe . Another disturbing factor is that the images do not cover exactly the same area, which causes Δe to differ from image to image.

Note that the minimum apparent temperature observed during the measurements is only 190.9 K, although blank metal objects (like the strip) are included in the scene. According to⁸, the minimum detectable temperature of the video-detector is 184 K (= noise level of the detector). This seems to be in accordance with our observed minimum.

5. Conclusions and recommendations

Conclusions:

- the buried mines were invisible at any time
- the AP mines were invisible at any time due to their small size
- the plastic AT mines were visible, and were at any time brighter than the sand background (positive contrast without contrast inversion)
- the metal AT mines were visible, and were at (almost) any time darker than the sand background (negative contrast without inversion)
- the contrast of the visible mines decreases with increasing sky temperature (increasing cloud cover and rain intensity). The contrast reduction is larger for metal than for plastic mines.
- the painted metal mines have possibly an emissivity (0.81 ?) that is significantly larger than that of blank metal.

Recommendations:

- because the sky temperature influences mine contrasts heavily, a sky scan should be measured before and after each image
- a direct comparison between painted and unpainted metal mines should be performed

5. Acknowledgements

We thank F.A. Nennie and A. Plugge for their help with the radiometer hardware and the experiment. We are grateful to the Electro-Optics group of TNO-FEL for their support during the experiment. The discussions with S. English (Meteorological

office Bracknell, UK), L. Yujiri (TRW, USA) and P. de Maagt (ESA/ESTEC, NL) were of help for the data analyses. The work was performed under contract for the Royal Netherlands Army.

6. References

- [1] "Passive millimeter wave sensors for detection of buried mines", L. Yujiri, B. Hauss and M. Shoucri, In Proc. SPIE Aerosense, "Detection Technologies for Mines and Minelike Targets", June 1995, pp. 2-6
- [2] "Microwave radiometry for detection of metallic targets", K. Keskinen, L.V. Allan, P. Nguyen and Y. Das, Specialist Meeting on Microwave Radiometry and Remote Sensing Applications, E.R. Westwater (Ed.), Wave Propagation Laboratory, Boulder, Colorado, June 1992, pp. 182-186
- [3] "Detection of surface laid and buried mines with IR and CCD cameras, an evaluation based on measurements", Y.H.L. Janssen, A.N. de Jong, H. Winkel and F.J.M. van Putten, Proc. SPIE Aerosense, "Detection and Remediation Technologies for Mines and Mine-Like Targets", 1996
- [4] "Microwave remote sensing", F.T. Ulaby, R.K. Moore and A.K. Fung, Vol. I, II and III, Artech House, Inc., Reading, 1981
- [5] "Radar Handbook", M.I. Skolnik (Ed.), McGraw-Hill, New York, 1970, Ch. 39 "Passive detection"
- [6] "Microwave radiometry for minefield detection", K.J. Keskinen, L.E. Allan, P. Nguyen and P. Foley, MPB report 17-91, April 1991
- [7] "Adaptive filtering for image enhancement", T. Peli and J.S. Lim, Optical Engineering, 21(1):108-112, 1982.
- [8] "Radiometry: environmental influences, image processing and measurement results", G.J.M. Janssen and F.J. Klumpers, January 1989, TNO-FEL report no. 1989-33.
- [9] "Passive microwave signatures of landscapes in winter", C. Mätzler, Meteorol. Atmos. Phys., Vol. 54, pp.241-260, 1994
- [10] "Passive millimeter-wave imaging", S.K. Young, R.A. Davidheiser, B. Hauss, P.S.C. Lee, M. Mussetto, M.M. Shoucri and L. Yujiri, Quest, vol. 13, nr. 2, winter 1990/1991, pp. 2-21